THE JOURNAL OF PHYSICAL CHEMISTRY A
A JOURNAL OF THE AMERICAN CHEMICAL SOCIETY

pubs.acs.org/JPCA

Article

Constructing Multiresonance Thermally Activated Delayed Fluorescence Emitters for Organic LEDs: A Computational Investigation

Sanyam,[†] Rudranarayan Khatua,[†] and Anirban Mondal*

Cite This: *J. Phys. Chem. A* 2023, 127, 10393−10405

Read Online

ACCESS | Metrics & More | Article Recommendations | Supporting Information

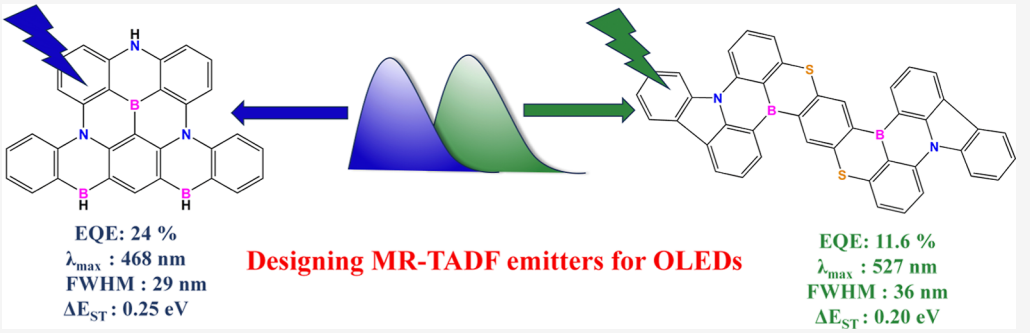

ABSTRACT: Multiple resonance thermally activated delayed fluorescence (MR-TADF) materials have acquired substantial attention due to their high electroluminescence efficiency with narrow emission spectra. However, the existing MR-TADF emitters suffer from substantial efficiency roll-off due to insufficient rate constants of the reverse intersystem crossing (k_{RISC}) process compared to the traditional TADF materials. Herein, we employ the DLPNO-STEOM-CCSD method, which is computationally less expensive than the wave function-based EOM-CCSD method, to evaluate the electronic and photophysical properties of MR-TADF materials accurately. The predicted singlet−triplet energy gap (ΔE_{ST}), one of the critical parameters governing the TADF efficiency, exhibits remarkable agreement with the experimental measurement, with a standard deviation value of 0.026 eV (obtained based on five experimentally synthesized MR-TADF systems). The proposed technique was utilized to determine the suitability of 15 newly designed MR-TADF emitters via their computed radiative and nonradiative rates, luminescence efficiencies, and exciton characteristics. Moreover, most conceived molecules exhibit blue emission with decent to strong oscillator strengths, making them potential candidates for practical light-emitting applications. The proposed computational route will undoubtedly accelerate the designing and prescreening of potential MR-TADF emitters before their expensive laboratory synthesis and characterization.

1. INTRODUCTION

External quantum efficiencies of organic light-emitting diodes (OLEDs) are limited by the unfavorable spin statistics of molecular excited states. In the case of OLEDs, charge carriers recombine to yield singlet and triplet excited states in a 1:3 ratio. Due to the spin-forbidden nature of triplet excited states to emit photons, OLEDs suffer severe limitations in the internal and external quantum efficiencies and energy loss. To overcome this challenge, two independent strategies have been established to harvest dark triplet excited states as photons. The first comprises organometallic complexes with transition metals, which render a sizable spin−orbit coupling to allow triplet states to emit via phosphorescence.[1−3] The latter relies on fluorescence materials based on the principle of thermally activated delayed fluorescence (TADF) with 100% exciton utilization.[4−6] Due to a pure organic-based molecular architecture and almost 100% internal quantum efficiency (IQE), TADF emitters are superior to fluorescent molecules that can use only 25% of excitons in terms of IQE and have the advantage of a low-cost alternative to phosphorescent organometallic complexes containing expensive precious metals such as iridium and platinum.

The efficiency of the TADF mechanism relies on close-lying singlet and triplet excited states in which ambient thermal energy upconverts the triplet states into singlet states through reverse intersystem crossing (RISC). In addition, a significant transition dipole moment between the first singlet excited state (S_1) and ground state (S_0) is required to accelerate the rate of $S_1 \rightarrow S_0$ fluorescence. Experimentally, these requirements are

Received: July 27, 2023
Revised: November 14, 2023
Accepted: November 17, 2023
Published: December 4, 2023

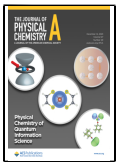

https://doi.org/10.1021/acs.jpca.3c05056
J. Phys. Chem. A 2023, 127, 10393−10405

commonly accomplished by employing a twisted donor−acceptor (D−A) molecular architecture that promotes the separation of the highest occupied molecular orbital (HOMO) and lowest unoccupied molecular orbital (LUMO) for minimized orbital overlap.[5,7−11] The localization of the electron density on the donor and acceptor moieties yields a reduced singlet−triplet energy gap (ΔE_{ST}), consequently facilitating RISC from the first triplet excited state (T_1) to S_1. However, there are several disadvantages associated with the twisted D−A-type molecular architecture.[6,12,13] First, due to the small exchange integral between HOMO and LUMO, the oscillator strength for the $S_1 \rightarrow S_0$ transition is minimal, which negatively impacts the device efficiency by reducing the photoluminescence quantum yield (PLQY). Second, the emission from TADF compounds is typically broad (0.45−0.55 eV; 80−110 nm) due to the stabilization of the intramolecular charge transfer (ICT) excited state for singlet emission. The broad emission leads to a poor color purity in the device, which requires an optical filter to remove unnecessary colors, leading to a significant energy loss. Third, owing to the large structural relaxation in the excited states and vibronic coupling between the ground and excited states, TADF emitters exhibit significant Stokes shifts.

Recently, Hatakeyama and co-workers reported an alternative strategy to address the limitations of conventional TADF emitters by introducing multiple resonance (MR)-based TADF compounds with boron- and nitrogen-embedded planar and rigid polycyclic molecular structures.[14] The MR effect is induced by the opposite resonating features of nitrogen and boron atoms, triggering alternating HOMO and LUMO distributions on different carbon atoms in the same aromatic ring of the emitter molecule.[8,15−18] A rigid framework combined with the MR effect successfully suppresses the vibronic coupling between the $S_1 \rightarrow S_0$ transition, realizing a narrow full width at half-maximum ($fwhm$) and a small Stokes shift (<30 nm), yielding a low reorganization energy and a high PLQY. In addition, the oscillator strength and color purity are significantly improved due to the high degree of HOMO and LUMO overlap within the aromatic framework. Since the first report on the MR-TADF emitter, many studies have been devoted to structural modifications to improve the properties of the MR-TADF materials.[7,8,15,17−28] Despite having excellent characteristics, most MR-TADF compounds suffer from a low rate of RISC (k_{RISC}),[29] often around 10^4 s^{-1}. The slow k_{RISC} leads to a long-delayed fluorescence lifetime which is detrimental to device performance, with most OLEDs based on MR-TADF complex as an emitter suffering from significant efficiency roll-off.[14] Moreover, the fastest k_{RISC} observed in MR-TADF-based emitters are in the order of 10^6 s^{-1} and are nearly 2 orders of magnitude slower than that of the best-performing D−A-type conventional TADF emitter (~10^7 to 10^8 s^{-1}).[29] A significant factor in this apparent gap in k_{RISC} is that the chemical space explored for MR-TADF emitters is limited to the N−B−N skeleton and remains small compared with the thousands of conventional D−A-type compounds reported. Thus, a new chemical design strategy for novel chemical structures with color tunability is desired to achieve optimal efficiency.

Several theoretical and computational studies have attempted to demonstrate the TADF mechanism and determine RISC rates in MR molecules.[16,17,23,29−31] However, it is still challenging and difficult to accurately predict intersystem crossing (ISC) and RISC rates, which are governed by critical factors such as ΔE_{ST} and spin−orbit coupling (SOC) matrix elements.[32] In this regard, Pershin and co-workers demonstrated the shortcomings of time-dependent density functional theory (TD-DFT) methods for predicting the nature and energies of the excited singlet and triplet states in MR-TADF compounds.[17] They have further shown that the prediction accuracy of those essential parameters can be improved significantly by employing coupled-cluster computations, which account for double-excitation contributions but at a much higher computational cost.[23,33]

In this work, we employ a computationally efficient approach to estimate ΔE_{ST} and, subsequently, the rates of different photophysical events relevant to MR-TADF emitters. We choose the similarity-transformed equation of motion (STEOM) method[34,35] augmented with the domain-based local pair natural orbital (DLPNO) theory devised by Neese et al.[36−39] to compute the excited-state energy levels accurately. It has been demonstrated that the DLPNO-STEOM-CCSD method can adequately account for the higher-order excitations (singles and doubles) and hence offers an accurate treatment for the excited-state characteristics of various molecules, including TADF-based compounds.[40−43] Recently, Bredas and co-workers[44,45] investigated the sulfur- and selenium-incorporated MR-TADF emitters via the DLPNO-STEOM-CCSD method. Their results further showed the efficiency and good predictability of the method when compared to those of experimental measurements. We first validate our strategy by comparing ΔE_{ST} and various rates against the experimentally reported measurements for the MR-TADF molecules, B1−B5.[14,15,18,28,46] Later, we designed and tested 15 new MR-TADF emitters using the proposed method. Several of them showed remarkable k_{RISC}, with the emission colors ranging from blue to green with high oscillator strengths. The computational protocol presented in this study can be translated to future novel MR-TADF materials, so that more promising candidates can be efficiently explored.

2. COMPUTATIONAL DETAILS

2.1. Quantum Chemical Calculations. The ground-state geometries (S_0) of the investigated MR-TADF molecules were optimized at the B3LYP/6-311+G(d,p) level of theory. On the other hand, excited-state geometries (S_1 and T_1) were obtained via TD-DFT calculations, employing the ωB97XD/6-31g(d,p) method. As reported in the literature, the B3LYP method performs well for the ground-state structural and electronic properties.[47] Contrarily, the range-separated ωB97XD functional was demonstrated as an appropriate choice for geometry optimization in the excited state.[48] Employing the B3LYP method for the ground-state optimizations reduces the computational cost over similar calculations if performed using the ωB97XD functional. These differences led us to choose the two ground- and excited-state calculation methods. TD-DFT calculations were performed using a conductor-like polarizable continuum model (CPCM),[49] with toluene (ϵ = 2.4) as a solvent for all the investigated systems. These calculations were carried out using the Gaussian 09[50] program suite. To accurately compute the excited-state energy levels, ΔE_{ST}, the spin−orbit coupling, and reorganization energies, we performed DLPNO-STEOM-CCSD calculations in combination with the def2-SVP basis set, as implemented in the ORCA program, v.5.0.[51] The def2-SVP basis set was used for our calculations primarily to reduce the overall computational cost. We tested the convergence of the cutoff values used for the

https://doi.org/10.1021/acs.jpca.3c05056
J. Phys. Chem. A 2023, 127, 10393−10405

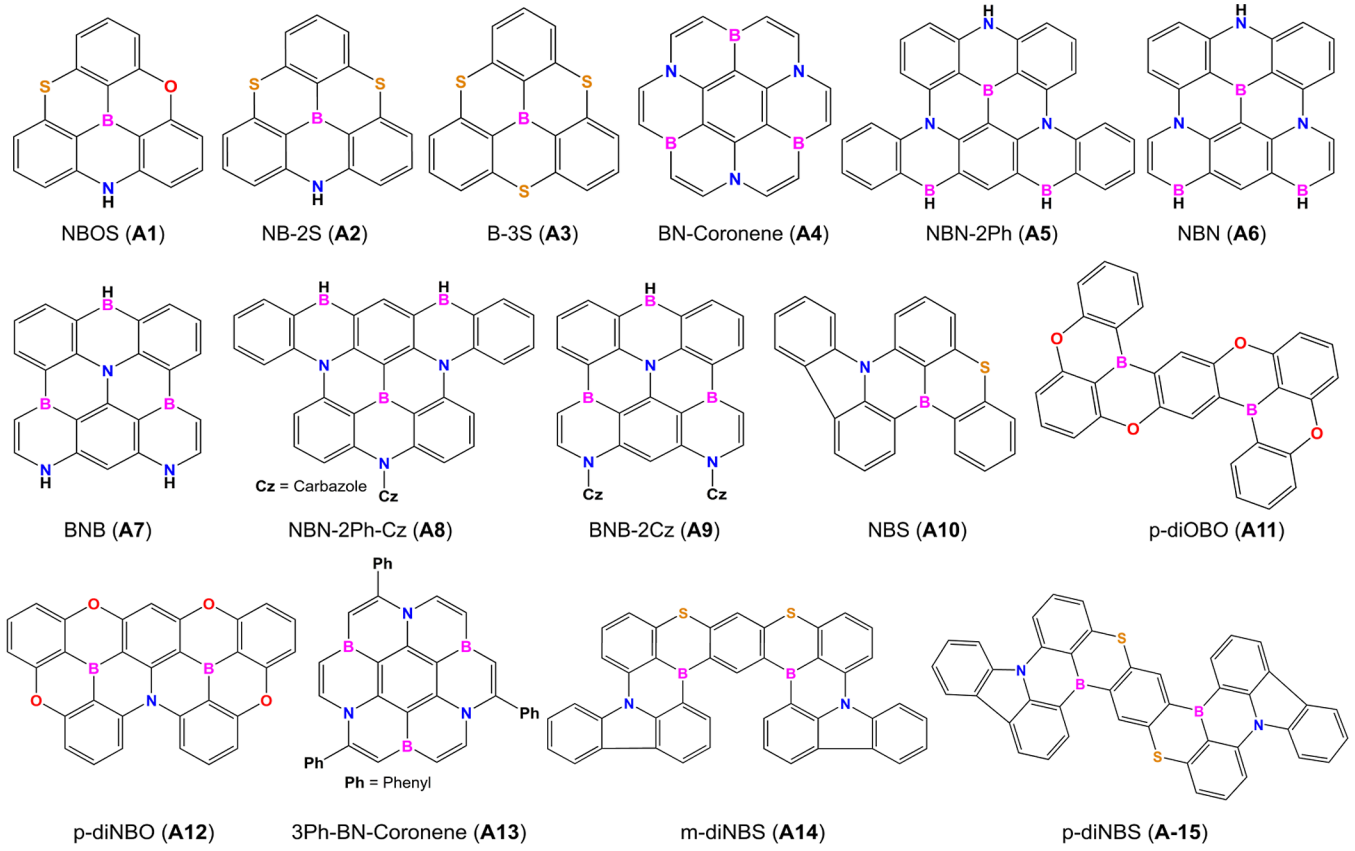

Figure 1. Chemical structures of the designed MR-TADF emitters in the present study.

DLPNO-STEOM-CCSD calculation. The converged cutoff values used were othresh = 0.005, vthresh = 0.005, and TCutPNOSingles = 10^{-11}. ΔE_{ST} values were estimated from the vertical excitation energies employing DFT-predicted ground-state (S_0) optimized geometries. However, the excited-state geometries (S_1 and T_1) at the TD-DFT level were utilized to compute reorganization energies. The DLPNO-STEOM-CCSD calculations considered the CPCM solvent model, with toluene (ϵ = 2.4) as the solvent.

2.2. Materials Design Strategy. Material selection and design play a vital role in acquiring lower ΔE_{ST} and, subsequently, efficient TADF output. Hatakeyama et al.[14] introduced the boron-embedded B−N framework in which the boron atom functions as the electron-withdrawing group due to its vacant p orbital. Notably, the N center can be replaced with other heteroatoms like O and S. For example, Chen et al. developed polycyclic aromatic hydrocarbons doped with B and S atoms that showed excellent MR-TADF properties.[52] Within the MR-TADF framework, the lone pairs of heteroatoms (N, O, and S) act as the electron-donating group. As a result, the resonance effect yields well-separated HOMO and LUMO distributions in the molecular system. In addition, a rigid architecture ensures minimum vibronic coupling, which further helps the molecule to emit in a narrow range with adequate color purity. In this case, the relative position of the boron atom to the heteroatoms is an essential parameter to consider, as it tends to govern the weak or strong conjugation effect, which regulates the emission wavelength.

Following the above approach with added flavors of chemical intuition, we have designed 15 new MR-TADF molecules, as depicted in Figure 1. Compounds A1−A3 are designed by including S or N atoms instead of O atoms in the triphenyl borane system reported in ref 53. The A4 compound originates from the coronene molecule with the inclusion of B and N atoms in alternating para positions. Substitution of the S atoms with N and fusion of a pair of naphthalene units at the peripheral benzene ring in the A2 complex yielded the A5 molecule. On the other hand, removing two phenyl rings in the end positions and including a carbazole unit link to the N-heteroatom of the parent A5 compound yielded A6 and A8, respectively. Molecule A7 is formed by exchanging the positions of the N and B atoms in the bare A6 system. In contrast, the A9 complex is designed by incorporating two carbazole units at the N-positions of the A7 compound. Besides these, we have devised a few fuzed MR-TADF molecules by substituting similar functional groups within the material, as illustrated in Figure 1. This fused structure aims to enhance the conjugation, alter the molecular orbital character, and influence their photophysical performances. In this category, A11 and A12 are assembled by fusing two OBO (5,9-dioxa-13-boranaphtho[3,2,1-de]anthracene) moieties at the para position with each other.[54] Modifications of the A1 system by the fusion of a carbazole group resulted in an A10 molecule. Consequently, A14 and A15 are constructed by extending the A10 system in the meta and para arrangements. In A14 and A15 complexes, the two boron atoms are placed relative to each other in the meta and para positions. In general, carbazole is a strong donor, which may influence the molecular geometry and, subsequently, the ΔE_{ST} value of the compounds. We aim to study the effect of the carbazole unit as a substituted compound (A8) and fused compound (A15). Overall, our strategy to include sulfur can be justified as it

https://doi.org/10.1021/acs.jpca.3c05056
J. Phys. Chem. A 2023, 127, 10393−10405

exhibits a better electron-donating ability than oxygen, which may influence the π-conjugation. Also, we anticipate an improvement in spin−orbit coupling, which is directly dependent on the atomic number.

2.3. Photophysical Properties. The photophysical properties of the MR-TADF systems are examined via parameters such as rates of prompt fluorescence (k_{PF}), intersystem crossing (k_{ISC}), reverse intersystem crossing (k_{RISC}), internal quantum efficiency (IQE), external quantum efficiency (EQE), and photoluminescence quantum yields (PLQY). The details of the mathematical relations are discussed below.

2.4. Rate of Prompt Fluorescence. The rate of prompt fluorescence, which occurs due to the radiative decay from the first singlet excited state, can be estimated using Einstein's spontaneous emission equation.[55]

$$k_{PF} = \frac{\Delta E_{S_0S_1}^2 f_{S_0S_1}}{1.499} \quad (1)$$

Here, $f_{S_0S_1}$ is the oscillator strength, and $\Delta E_{S_0S_1}$ is the energy difference between S_0 and S_1 states in cm^{-1}.

2.5. Rate of Intersystem and Reverse Intersystem Crossing. The stable triplet state (T_1) below the first singlet excited state (S_1) and the small value of ΔE_{ST} ensure that the exciton may go into the triplet state by the intersystem crossing. The reverse phenomenon involving uphill energy as the activation energy is also possible, known as reverse intersystem crossing. The rate constants of ISC (from S_1 to T_1) and RISC (from T_1 to S_1) were estimated within the framework of Fermi's golden rule[56]

$$k_{(R)ISC}^{IF} = \frac{2\pi}{\hbar} |\langle 1\psi_I^0 | H_{SO} | {}^3\psi_F^0 \rangle|^2 [FCWD] \quad (2)$$

Here, I and F denote the initial and final excited states; FCWD represents the Franck−Condon weighted density of states, and $\langle {}^1\psi_I^0 | H_{SO} | {}^3\psi_F^0 \rangle$ defines the spin−orbit coupling. The FCWD term can be described classically in the high-temperature limit

$$FCWD = \frac{1}{\sqrt{4\pi\lambda k_B T}} \exp\left[- \frac{(\Delta E + \lambda)^2}{4\pi\lambda k_B T} \right] \quad (3)$$

Here, λ is the total reorganization energy, and ΔE is the energy difference between the initial and final states, which is nothing but ΔE_{ST} in this subject. The transition rate between S_1 and T_1 (vice versa) was determined by three key parameters: the spin−orbit coupling ($H_{SO}^{S_1T_1}$), the energy difference between the two states, ΔE_{ST} (the sign is opposite for RISC and ISC), and reorganization energy λ, where k_B is the Boltzmann constant, $\hbar$ is the reduced Planck's constant, and T is the room temperature (298 K). Large spin−orbit coupling and small coupling ($\Delta E_{ST} + \lambda$) are advantageous for these processes. Organic semiconductors' reorganization energy comprises two components—internal (λ_i) and outer (λ_s) reorganization energies. While the internal reorganization energy is computed via the standard four-point approach, which is also applied here, the outer-sphere contribution due to the solvation effect is generally considered an added term to the total. We have followed a similar protocol as reported in the literature[56,57] and considered 0.2 eV toward the outer-sphere contribution to the total reorganization energy. On the other hand, the DLPNO-STEOM-CCSD method was employed to estimate the internal reorganization energy, considering toluene as the solvent. The inner reorganization energies (λ_i) are computed via the following expressions

$$\lambda_{ISC} = E_{T_1(S_1)} - E_{T_1(T_1)}$$
$$\lambda_{RISC} = E_{S_1(T_1)} - E_{S_1(S_1)} \quad (4)$$

Here, $E_{T_1(S_1)}$ is the T_1 state energy in S_1 geometry, and $E_{T_1(T_1)}$ is the T_1 state energy in T_1 geometry. On the other hand, $E_{S_1(T_1)}$ is the S_1 state energy in T_1 geometry, and $E_{S_1(S_1)}$ is the S_1 state energy in S_1 geometry.

2.6. Rate of Delayed Fluorescence. The TADF mechanism usually involves two steps: (i) transfer of triplet excitons to the singlet state via RISC and (ii) radiative fluorescence from the singlet state to the ground state. Thus, the time taken for the whole process of the TADF phenomenon is equal to the sum of the time the excitons take for RISC and fluorescence. The rate constant is defined theoretically in the following equation[58]

$$k_{TADF}^{-1} = \tau_{TADF} = k_{PF}^{-1} + k_{RISC}^{-1} \quad (5)$$

Detailed mathematical expressions employed to assess IQE, EQE, and PLQY are provided in Supporting Information.

3. RESULTS AND DISCUSSION

3.1. Validation of the Proposed Computational Strategy. *3.1.1. Singlet−Triplet Energy Gap.* ΔE_{ST} is one of the critical parameters in determining the rates of ISC and RISC and, consequently, the TADF efficiency. However, obtaining an accurate estimation of ΔE_{ST} using computational methods has been challenging. Pershin et al. have demonstrated that for MR-TADF systems, TD-DFT methods often yield an overestimation of ΔE_{ST} compared to experimental measurement.[17] As a remedy to this drawback, they have used the spin-component-scaling second-order approximate coupled-cluster (SCS-CC2) method, which outperformed TD-DFT for predicting ΔE_{ST}.[59] More recently, Shizu and Kaji demonstrated the efficacy of the equation-of-motion coupled-cluster single and double (EOM-CCSD) method in describing the excited-state characteristics of the MR-TADF molecule, DABNA-1.[60] Their results showed a significant improvement in the estimation of ΔE_{ST} relative to those reported via TD-DFT methods. Although both SCS-CC2 and EOM-CCSD approaches showed improved accuracy in ΔE_{ST} prediction due to the (partial) inclusion of double excitations, the computational cost associated is significantly larger than that associated with the TD-DFT computations. As a result, performing many SCS-CC2 or EOM-CCSD calculations required screening of molecules from a vast set of potential MR-TADF molecules which becomes tedious.

Unlike the abovementioned wave function-based methods, the DLPNO-STEOM-CCSD approach can efficiently represent charge transfer states and predict ΔE_{ST} at a lower computational cost without compromising the accuracy of the EOM-CCSD or SCS-CC2 method.[40−42] The computational overhead was the primary reason for estimating ΔE_{ST} using the vertical T_1−S_1 energy difference, as optimizing each emitter's S_1 and T_1 geometries at the DLPNO-STEOM-CCSD level is challenging and requires high computational costs. A similar approach to determine ΔE_{ST} from vertical S_1 and T_1 energies was reported in refs 44, 45, and 59. The performance of the DLPNO-STEOM-CCSD method in predicting singlet−triplet gaps in the azine derivatives was recently reported in ref 43.

https://doi.org/10.1021/acs.jpca.3c05056
J. Phys. Chem. A 2023, 127, 10393−10405

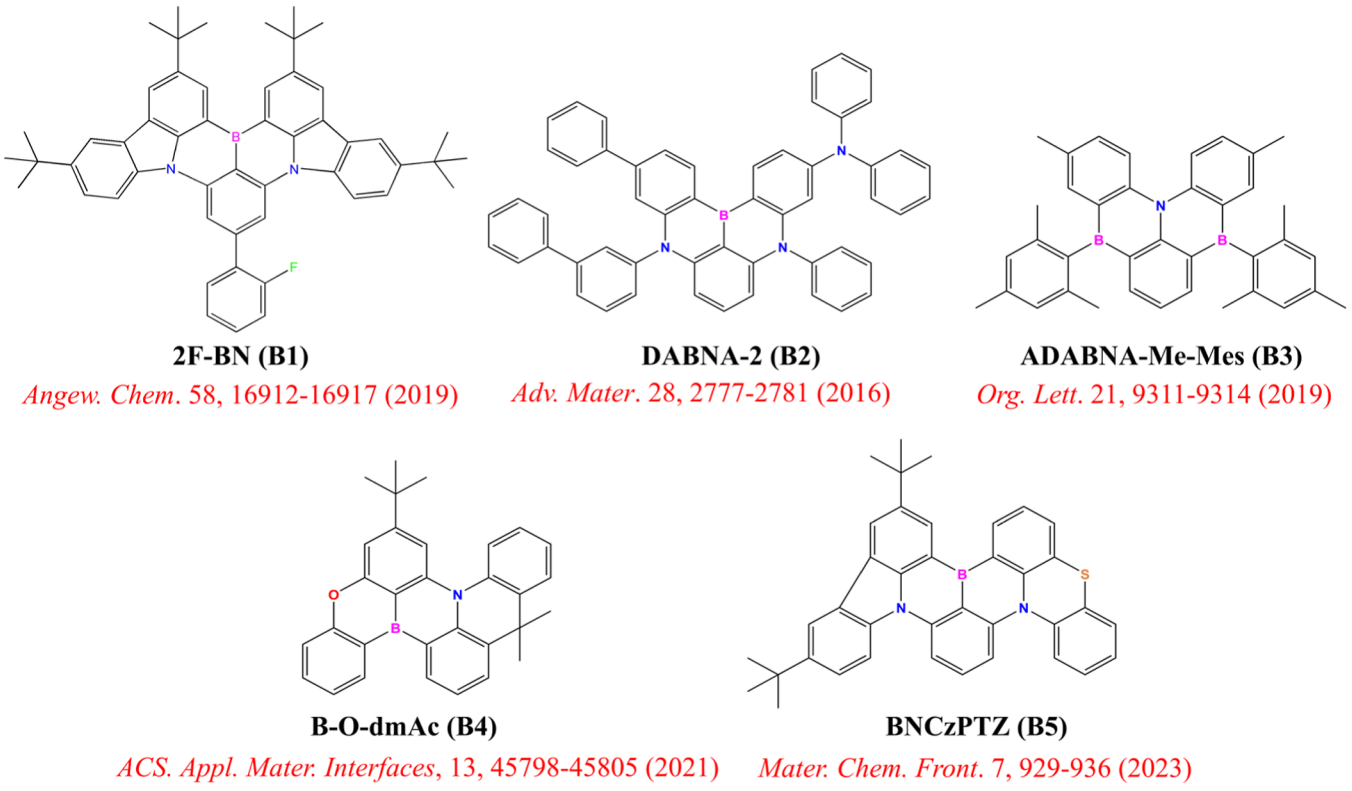

Figure 2. Chemical structures of the experimentally reported MR-TADF emitters.

Table 1. Comparison between Experimental and Simulated E_{S_1}, E_{T_1}, ΔE_{ST}, Spin−Orbit Coupling (H_{SO}), Rates, EQE, and PLQY in the MR-TADF Complexes, B1,[18] B2,[14] B3,[15] B4,[28] and B5[46a]

quantity	B1	B2	B3	B4	B5
E_{S_1} [eV]	2.654 (2.51)	2.918 (2.71)	2.879 (2.59)	2.920 (2.77)	2.709 (2.61)
E_{T_1} [eV]	2.487 (2.35)	2.734 (2.56)	2.659 (2.39)	2.749 (2.66)	2.579 (2.52)
ΔE_{ST} [eV]	0.167 (0.16)	0.184 (0.15)	0.220 (0.20)	0.171 (0.11)	0.130 (0.09)
H_{SO} [cm^{-1}]	0.08	0.07	0.05	0.04	0.02
k_{PF} [s^{-1}] × 10^8	1.14 (0.56)	1.96 (1.14)	1.08 (1.00)	0.96 (1.41)	1.31 (0.25)
k_{ISC} [s^{-1}] × 10^7	0.51 (1.49)	0.14 (1.01)	0.14 (2.90)	0.11 (7.16)	1.87 (2.11)
k_{RISC} [s^{-1}] × 10^5	4.20 (0.22)	2.68 (0.15)	0.92 (0.08)	1.19 (0.18)	51.4 (1.54)
k_{TADF} [s^{-1}] × 10^5	4.17	2.68 (0.15)	0.92 (0.06)	1.19 (0.08)	49.50 (0.30)
EQE [%]	24.3 (22.0)	24.9 (20.2)	24.9 (16.2)	24.8 (16.2)	22.9 (25.7)
PLQY [%]	99.8 (88.7)	100.0 (90.0)	100.0 (89.0)	100.0	98.4 (91.0)

[a]The experimental numbers, wherever available, are given in parentheses.

Also, Bredas and co-workers performed DLPNO-STEOM-CCSD calculations on chalcogen-substituted MR-TADF emitters.[44,45] They found that the predicted ΔE_{ST} values were in satisfactory agreement with the experimental measurements. Thus, to get accurate ΔE_{ST} values for the MR-TADF molecules, we employ the DLPNO-STEOM-CCSD method in this study. We chose a set of experimentally reported well-known MR compounds (B1−B5) for validation (see Figure 2).[14,15,18,28,46] The vertical $T_1 \rightarrow S_1$ energy difference computed at the DLPNO-STEOM-CCSD/Def2-SVP level of theory was compared against the experimental ΔE_{ST} values. The computed values are given in Table 1. Our results revealed a mean absolute difference of 0.026 eV between the experiment and simulated data. A recent work by Hall and co-workers[59] demonstrated that the SCS-CC2 method yields mean absolute deviations of 0.55 and 0.56 eV for S_1 and T_1 energy levels compared to experimental measurements. Our calculations show that the DLPNO-STEOM-CCSD method also overestimates both S_1 and T_1 energies. However, compared to SCS-CC2, the mean absolute deviation is lower, −0.15 and 0.18 eV, for S_1 and T_1 states, respectively. Such a minor deviation for a set of five compounds gives us the confidence to employ the DLPNO-STEOM-CCSD/Def2-SVP method to study the designed MR-TADF complexes.

3.1.2. Rate Constants and Luminescence Quantum Efficiencies. To continue with our validation, we evaluated the rates of different photophysical events in eqs 1 and 2. The predicted rates and quantum efficiencies are compared against the available experimental measurements for the five tested compounds; the results are summarized in Table 1. The computed reorganization energies and ISC and RISC rates considering the contribution from the T_2 state in complexes B1−B5 are tabulated in Tables S1 and S3 of the Supporting Information. As can be seen from Table S3, both k_{ISC} and k_{RISC}

https://doi.org/10.1021/acs.jpca.3c05056
J. Phys. Chem. A 2023, 127, 10393−10405

Table 2. Computed Emission Wavelength (λ, nm), ΔE_{ST} (eV), Rates (in s^{-1}) of $k_{PF} \times 10^8$, $k_{ISC} \times 10^7$, $k_{RISC} \times 10^5$, and $k_{TADF} \times 10^5$, EQE (%), and PLQY (%) for the Designed Compounds Studied in this Work

system	λ	ΔE_{ST}	k_{PF}	k_{ISC}	k_{RISC}	k_{TADF}	EQE	PLQY
A1	402.5	0.273	0.66	2.29	8.39	8.28	17.9	88.5
A2	431.9	0.195	0.58	3.00	45.10	41.80	14.4	75.0
A3	433.3	0.248	0.48	1.03	4.61	4.57	20.9	95.6
A4	375.2	0.063	1.84	6.08	294.00	253.00	27.7	100.0
A5	468.0	0.247	0.81	0.46	2.36	2.35	24.0	99.7
A6	438.3	0.340	1.24	0.38	0.42	0.42	24.4	99.9
A7	434.1	0.288	1.03	1.20	67.80	63.60	23.9	99.3
A8	453.2	0.243	1.04	58.50	265.00	211.00		
A9	420.2	0.268	1.30	0.47	19.30	19.00	24.6	99.9
A10	448.7	0.230	1.20	9.86	99.20	91.60	5.8	34.2
A11	446.1	0.292	0.94	0.05	1.24	1.23	24.9	100.0
A12	411.5	0.244	1.42	0.64	51.80	50.00	24.8	100.0
A13	391.5	0.127	8.16	6.08	104.00	103.00	23.8	99.5
A14	448.0	0.097	0.99	2.22	263.00	208.00	24.6	99.6
A15	527.5	0.201	1.05	6.33	4.19	20.70	11.6	64.3

rates differ significantly compared to the experiment when the T_2 contribution is considered. This implies that the T_1 contribution is the major one during the investigation of these rates. As is evident from Table 1, the predicted rates are in satisfactory agreement with the experimentally obtained rates. Computed rates for k_{PF} slightly deviate from the experimental rates by an order of magnitude or even less than that. For the ISC rate, the predicted value often underestimated the experimental one by an order of magnitude, with a maximum deviation of 65 times for the B4 complex. Similarly, for k_{RISC}, the computed values are overestimated by an order of magnitude except for the B5 compound, with a maximum deviation of 33 times compared to the experiment. In addition, the estimated EQE value shows excellent agreement with the experiment. Important to note is that the spin−orbit coupling and reorganization energies are computed via the DLPNO-STEOM-CCSD method, considering the emitter in an implicit solvent model, with toluene as the solvent. Differences in the environmental conditions may play a vital role in the observed marginal difference between the predicted and experimental rates. These correlations thus validate our computational approach and further ensure its transferability for determining ΔE_{ST}, rates, and efficiencies for the newly designed compounds.

3.2. Performance of the Designed MR-TADF Emitters.

With the aid of the DLPNO-STEOM-CCSD calculations, we obtained ΔE_{ST} values in the newly designed compound, as shown in Figure 1. The computed ΔE_{ST} values are summarized in Table 2. As is evident from Table 2, most of our designed MR-TADF molecules possess ΔE_{ST} below 0.3 eV, with the maximum predicted result of 0.34 eV. To assess the quality and performance of the designed MR-TADF molecules, evaluating and analyzing the rates of photophysical processes and luminescent efficiencies are necessary. We determined these rates and quantum efficiencies for all of the investigated systems using eqs 1−5. Spin−orbit couplings and the reorganization energies (obtained via eq 4) associated with the $S_1 \leftrightarrow T_1$ transitions are tabulated in Table S1 of the Supporting Information. Table 2 summarizes the computed rates and efficiencies for the designed MR-TADF complexes.

Table 2 shows that the predicted rates in the newly designed compounds are significantly improved compared with the existing MR-TADF emitters. Except for a couple of systems, all the designed emitters possess EQE and PLQY above 20 and 90%, respectively. Among the 15 complexes, k_{PF} (k_{ISC}) consistently turns out to be in the range 10^8 s^{-1} (10^7 s^{-1}). However, k_{RISC} and k_{TADF} exhibit a range of values—in the span of 10^4 to 10^7 s^{-1}. The variation in k_{RISC} may originate from the difference in the associated reorganization energies, an essential element in the Marcus equation. A careful inspection revealed that the symmetric compound A4 possesses the smallest ΔE_{ST} value with enhanced rate constants and significantly larger EQE and PLQY. Compounds A1, A2, and A3 are slight modifications of the experimental structures. While A1 and A3 show balanced rate constants and luminescence quantum efficiencies, A2 performs slightly poorer in terms of EQE and PLQY. This is due to the larger magnitude of the k_{ISC}/k_{PF} ratio, which is detrimental to quantum efficiencies. For compounds A2 and A3, the spin−orbit coupling corresponding to S_1-T_1 transition was zero. Thus, we considered the transition from the T_2 contribution, and the corresponding rates are tabulated in Table 2. Similarly, the T_2 contribution was considered for complexes A7 and A9. Compounds A6 and A7 are only different regarding the relative positions of boron and nitrogen atoms. B and N centers are linked to the para positions, with one boron atom at the center in the case of A6, whereas it is nitrogen for A7. Although k_{RISC} and k_{TADF} are 2 orders of magnitude higher in A7, both EQE and PLQY remain almost the same in both complexes. This comparison shows that slight geometrical modifications in the architecture do not alter the overall performance of these emitters. Moreover, complex A5, simply a phenyl-fused derivative of A6, exhibits rate constants and quantum yields similar to those of A6 or A7. The compounds A8 and A9 demonstrate the effect of carbazole substitution on compounds A5 and A7, respectively. Although ΔE_{ST} is slightly improved in A9, the overall rates and quantum yield remain almost the same as in A7. On the contrary, a similar substitution in A5 degraded the overall performance, as seen in the A8 complex; k_{ISC} is greater than the prompt fluorescence rate, leading to negative quantum yields. In a similar line, compounds A10 and A13 display excellent k_{RISC} and k_{TADF} rates and superior quantum yields. Finally, except for A15, the remaining systems display excellent rates and quantum yields in the fused complexes. Among these complexes, A14 possesses the lowest ΔE_{ST} and highest EQE and PLQY. Similar to the A2 system,

https://doi.org/10.1021/acs.jpca.3c05056
J. Phys. Chem. A 2023, 127, 10393−10405

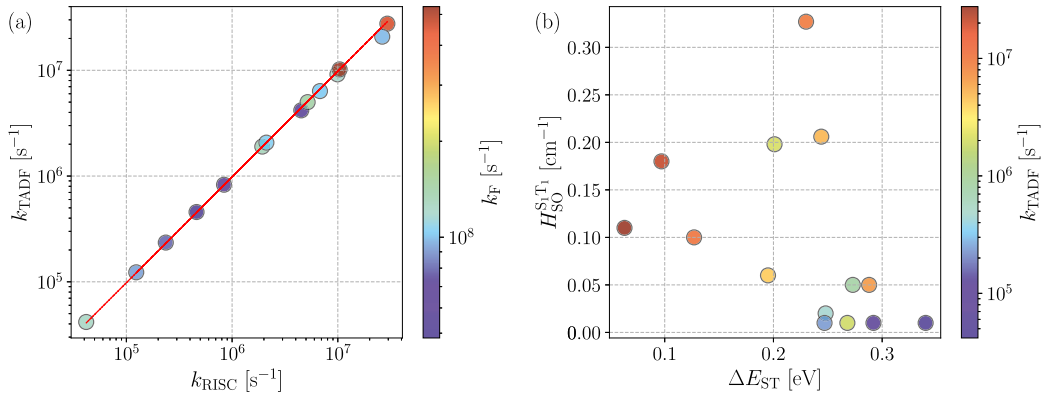

Figure 3. (a) Correlation plot between k_{RISC} and k_{TADF}. The color of each point represents the k_{PF} value. (b) Correlation plot between ΔE_{ST} and $H_{SO}^{S_1T_1}$. The color of each point represents the k_{TADF} value.

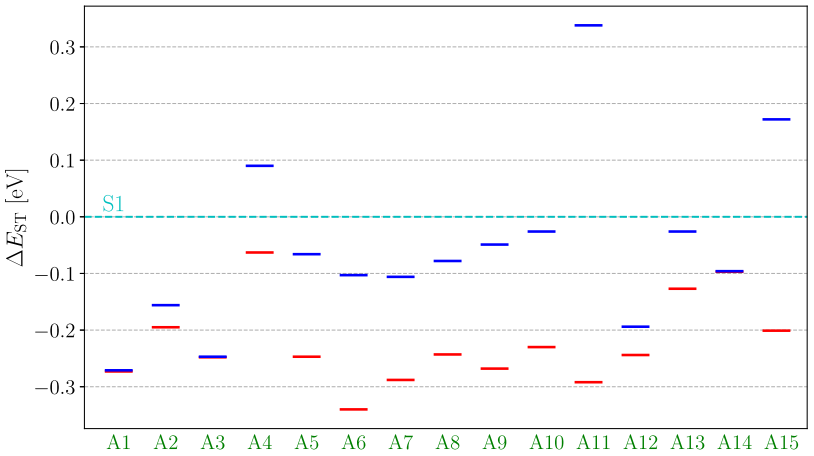

Figure 4. Relative positions of T_1 (red) and T_2 (blue) states with respect to the S_1 (cyan dotted line) state in the designed MR-TADF complexes.

due to the larger magnitude of the k_{ISC}/k_{PF} ratio, A15 performs inferior to other fused emitters designed in this study. The carbazole unit directly fused in the core of A15 helps to elongate the π-conjugation, resulting in enhanced absorption wavelength and reduced ΔE_{ST} value compared to A8. Thus, the results exhibit that the fused form (A15) performs better than the substituted form (A8). Also, the thought behind introducing the sulfur atom is well justified by the more electron-donating ability of the sulfur atom in comparison to nitrogen and oxygen. Another advantage is that spin−orbit coupling is directly dependent on the atomic number—as a result, we observed large spin−orbit coupling in sulfur-containing systems, such as A10, A14, and A15, as tabulated in Table S1.

We further explore the essential relationships between the rates of different processes. Figure 3a shows the correlation between k_{RISC} and k_{TADF}, where each point is color-coded as per the magnitude of k_{PF}. The rate of delayed fluorescence grows linearly as there is an increase in the reverse intersystem crossing. On the other hand, k_{PF} remains 10^7 s^{-1} or higher throughout all the systems. It is important to note that both k_{ISC} and k_{RISC} are governed by ΔE_{ST} and the magnitude of spin−orbit coupling. In order to achieve an efficient delayed fluorescence, the T_1 to S_1 conversion must be more spontaneous (higher k_{RISC}) than the conversion in the opposite direction (lower k_{ISC}). One way to drive this process is by inducing triplet-to-singlet conversion from a higher-lying triplet state (but still small ΔE_{ST}) to the S_1 state, favoring the energetically downhill reverse intersystem crossing more than the S_1 to T_1 transfer via ISC. Therefore, one must pay extra attention when choosing functional groups or chromophores while designing new MR-TADF-based emitters.

It is a well-understood fact that an efficient TADF design relies on a smaller ΔE_{ST} value. In the literature, often, it has been reported that the threshold maximum for ΔE_{ST} should be at most 0.2 eV to achieve an efficient TADF device.[60] Figure 3b displays the correlations between ΔE_{ST} and $H_{SO}^{S_1T_1}$, where the color of each point represents the k_{TADF} value. In general, a higher rate is facilitated by a large SOC and a small ΔE_{ST}. Nevertheless, Figure 3b compares compounds having almost the same ΔE_{ST}, whereas the SOC is greater in one than in the other. Interestingly, the computed rates can be of a different order than the SOC. For example, two points are seen at ΔE_{ST} near 0.2 eV. This is possible only when other parameters, such as the reorganization energy, play a crucial role. As can be seen from Figure 3b (also summarized in Table 2), the designed MR-TADF emitters possess a ΔE_{ST} value in the range 0.06−0.34 eV. Except for compound A6, all other complexes exhibit k_{TADF} of 10^5 s^{-1} or higher, with a few in the range 10^7 s^{-1}. Such improved k_{TADF} rates are due to a significantly large spin−orbit coupling, $H_{SO}^{S_1T_1}$, between the S_1 and T_1 states. This observation indicates an important feature regarding the future TADF design—it is not always required to restrict ΔE_{ST} below 200 meV to accomplish an efficient TADF rate. Rather, it is essential to strike a balance between the magnitude of $H_{SO}^{S_1T_1}$

https://doi.org/10.1021/acs.jpca.3c05056
J. Phys. Chem. A 2023, 127, 10393−10405

and ΔE_{ST}, which combines to decide the fate of the efficiency of an (MR)-TADF emitter.

Another critical aspect, especially for the MR-TADF compounds, in determining ISC (RISC) rates is the route followed for the exciton transfer between singlet and triplet states. As Shizu and Kaji[60] demonstrated, often a higher lying triplet state (T_2 or T_3) may participate in ISC (RISC) events, primarily driven by their relative energetic positions with respect to the S_1 state as well as the corresponding spin−orbit coupling matrix elements. Figure 4 displays the locations of the T_1 and T_2 states along the energy scale relative to the S_1 state. As we observe, for most of the designed compounds, T_2 lies closer to the S_1 than that of the T_1 state. We further confirmed the locations of T_3 states in these complexes, which lie well above the S_1 state and are thus not considered for further analysis. A closer inspection reveals that for molecules A1, A3, and A14, the predicted T_1 and T_2 states are energetically almost the same, so there is not much difference in the ΔE_{ST} values. For complexes A5 to A10 and A12 to A14, the T_2 state lies below the S_1 state. In these cases, the T_2 state is much closer to the S_1 state compared to the T_1 state. On the contrary, for compounds A4, A11, and A15, the T_2 state stays above the S_1 state. For the complexes in which the T_2 state lies close to the S_1 state, the mechanism happens in a staircase manner, i.e., the exciton will go from the S_1 state to T_2 and then from T_2 to T_1 ($S_1 \leftrightarrow T_2 \leftrightarrow T_1$). Nevertheless, the associated spin−orbit coupling must be nonzero to materialize a $S_1 \leftrightarrow T_2$ transfer. For completeness, the computed $S_1 \leftrightarrow T_2$ spin−orbit coupling matrix elements and the k_{ISC} and k_{RISC} rates are summarized in Table S3 of the Supporting Information. Comparing Tables 2 and S3, we observe that the computed rates are comparable and determined by the relative magnitude of ΔE_{ST} and the associated spin−orbit coupling matrix elements.

Emission color: the emission characteristics of the designed MR-TADF systems are examined at the STEOM-DLPNO−CCSD/def2-SVP level of theory, including dichloromethane (ϵ = 8.9) as the solvent. Table 2 summarizes the emission wavelength values, whereas Table S1 of the Supporting Information lists the corresponding oscillator strengths. The designed molecules exhibit emission maxima in the 375−527 nm region, which translates to a violet to green color, as seen from Table 2. Except for the A15 molecule, the remaining systems are expected to exhibit blue emissions of different shades. The associated oscillator strengths (f) range from 0.13 to 1.20, implying a decent to quite strong fluorescence intensity. In the cases of A4 and A13, the oscillator strength for the $S_1 \rightarrow S_0$ transition is extremely low. The oscillator strengths of $S_1 \rightarrow S_0$, $S_2 \rightarrow S_0$, and $S_3 \rightarrow S_0$ are summarized in Table S6 of the Supporting Information. As seen from Table S6, the oscillator strength of $S_3 \rightarrow S_0$ is more significant than the other two transitions. The A4 and A13 compounds are the polyaromatic coronene-substituted compounds, in which the first two singlet-excited states (S_1 and S_2) are the dark states and S_3 is the first bright state, as illustrated in ref 61. These complexes are thus expected to emit from higher-lying excited states. Also, ref 62 demonstrated the emission regarding the high-lying emissive states for coronene and has shown that all three states are emissive, including S_1, S_2, and S_3. In order to gain a clearer insight into the emission in these two complexes, we have performed excited-state geometry optimization for the S_3 state. The S_3-optimized geometries of both A4 and A13 complexes are tabulated in Tables S7 and S8 of the Supporting Information. Considering these geometries, we computed the radiative rates for the S_3-to-S_0 transition using eq 1 of the paper. We compared them against the rates obtained for the S_1-to-S_0 transition in these two complexes. In the A4 emitter, the rate constant for the S_3-to-S_0 transition is 1.84×10^8 s^{-1} compared to 4.72×10^2 s^{-1} corresponding to the S_1-to-S_0 transition. Similarly, in A13, transition from S_3 and S_1 to the ground state S_0 possess rate constants of 8.16×10^8 and 3.96×10^5 s^{-1}, respectively. As is apparent, the fluorescence rate constant for the S_3-to-S_0 transition is much higher than that for the S_1-to-S_0 transition. In addition, the rate constant for the S_3-to-S_0 transition is in a similar order of magnitude of the fluorescence rates as seen in other complexes. These observations indicate that complexes A4 and A13 are expected to emit from a high-lying excited state, S_3 to S_0. The correlation between ΔE_{ST} and the emission wavelength, λ_{max}, is illustrated in Figure 5, where the color of each point depicts the

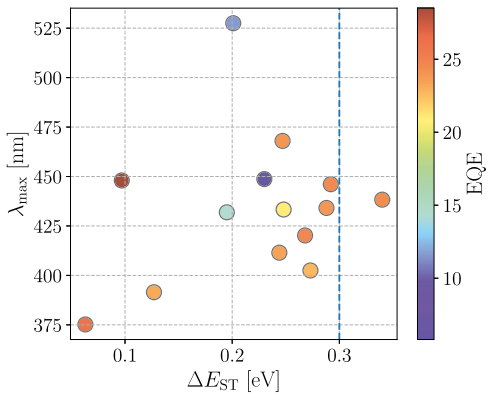

Figure 5. Correlation plot between ΔE_{ST} and emission wavelength, λ_{max}. The color of each point represents the EQE value.

corresponding EQE values. Most complexes have a λ_{max} value between 400 and 450 nm, implying a dark blue emission. Moreover, except for a couple of entities, all designed emitter molecules show significantly high EQE values, with magnitudes above 20%. Such uniformity in the EQE values is not always seen, considering that a few emitters possess a singlet−triplet energy gap larger than 0.2 eV. This observation again highlights the importance of balancing ΔE_{ST} and $H_{SO}^{S_1T_1}$—the two quantities regulating photophysical rates and luminescent efficiencies. These two quantities can, in principle, compensate each other, yielding highly efficient novel MR-TADF emitters. The above finding depicts the current computational approach's ability to tune the emission color with adequate oscillator strengths via a state-of-the-art, well-defined design strategy. Here, the strategy employed has generated a set of highly promising blue MR-TADF emitters, which are highly desired in the OLED industry. Further, to confirm the narrow band characteristics of the designed MR-TADF complexes, we computed the *fwhm* values. *fwhm* values were estimated using the Gaussian program[63] employing a combination of Lorentzian and Gaussian distributions. First, we have validated the simulated *fwhm* of the B1−B5 complex with the experimental measurements, as tabulated in Table S1 of the Supporting Information. As evident, the simulated *fwhm* values show adequate agreement with the experimental measurements. In addition, Table S1 of Supporting Information summarizes the *fwhm* values of the designed MR-TADF complex. As can be seen, the computed *fwhm* in the designed

https://doi.org/10.1021/acs.jpca.3c05056
J. Phys. Chem. A 2023, 127, 10393−10405

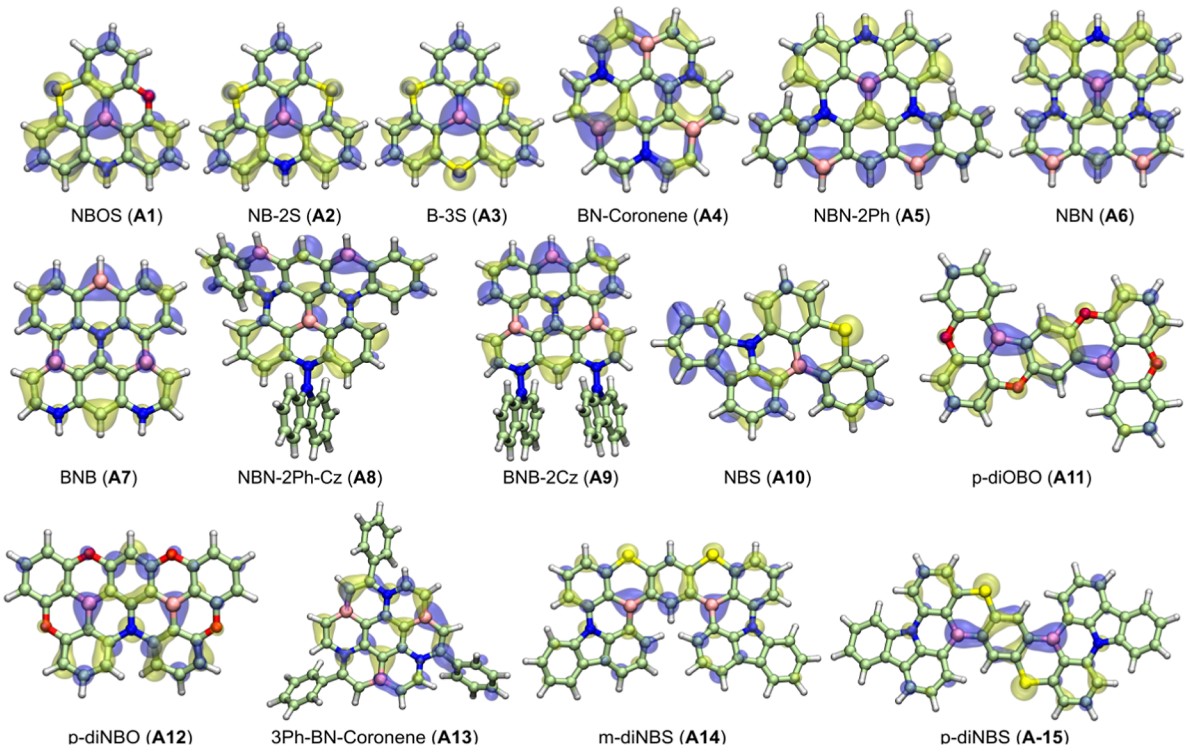

Figure 6. Frontier molecular orbital (HOMO in yellow and LUMO in blue) plot of the designed MR-TADF emitters in the present study.

MR-TADF complexes exhibits values similar to B1−B5, between 21.14 and 53.92 nm, implying the narrow band characteristics of the designed MR-TADF complexes. *fwhm* and molecular excited-state lifetime are generally associated via the Heisenberg uncertainty principle,[64] expressed via the following relation: $\Delta E \cdot \Delta t \geq \frac{\hbar}{2}$. The uncertainty principle limits the precision with which we can know the energy of a system (ΔE) and the time during which that measurement is made (Δt). In the context of spectral lines, the uncertainty principle implies a trade-off between the knowledge of the energy of a particle and the time over which that energy is known: the broader the *fwhm*, the shorter is the lifetime of the excited state and vice versa. The measured energy will have an extremely lower uncertainty in compounds with significantly larger excited-state lifetimes. It indicates that in delayed fluorescence complexes, the exciton resides in the excited state for an extended period. Consequently, the *fwhm* in these cases is reduced. Molecular size and rigidity are other molecular properties that can influence the *fwhm*. Larger, more rigid molecules, e.g., MR-TADF complexes, often have more closely spaced energy levels and exhibit narrower absorption bands. In contrast, traditional D−A−D compounds, possessing multiple flexible dihedrals, yield many conformations with varied excited-state energy levels responsible for their larger *fwhm* values.[65]

3.3. Frontier Molecular Orbitals. The distributions of molecular orbitals, HOMO and LUMO, are critical in deciding the magnitude of ΔE_{ST} and, consequently, the TADF efficiency in the materials that we are examining. The HOMO and LUMO distributions are shown in Figure 6. In an ideal design, HOMO and LUMO should be separated in space to minimize orbital overlap and render a reduced ΔE_{ST} value to promote efficient RISC from T_1 to S_1. D−A-type TADF emitters generally have well-defined donor−acceptor domains, where the donor and acceptor moieties are spatially separated. Contrarily, MR-TADF emitters lack the spatial separation of donor−acceptor with locally split electron-donating and electron-withdrawing groups. As illustrated in Figure 6, HOMOs are localized on the nitrogen and oxygen atoms as well as the ortho and para positions relative to both. On the other hand, LUMOs are distributed primarily on the boron atoms and at their meta and para positions. If the HOMO and LUMO are well separated with a minimal overlap, then the exchange interaction (β) is minimal; so, the singlet−triplet energy difference will also be small. In that case, the oscillator strength will be low with an increased S_0−S_1 energy gap, inducing blue-shifted absorption or emission.

3.4. Exciton Characteristics. To distinguish the exciton characteristics of the designed emitters, we evaluated three relevant descriptors, namely, D_{CT}, Q_{CT}, and $S_{\pm}$. These parameters were calculated based on the difference density plots employing the Multiwfn program.[66] The difference density plots, Δ, were obtained by using the following relation: $\Delta = \rho_{ex} - \rho_0$. Here, ρ_{ex} and ρ_0 represent the excited-state (S_1) and ground-state densities, respectively. Each of the three descriptors mentioned above provides an idea about the nature of the excitons. For example, D_{CT} measures the distance between the barycenter of ρ_+ and ρ_-, with increased and decreased electron densities. A larger D_{CT} (≥1.6 Å) accounts for the CT (charge transfer) character of the transition, whereas a LE (local excitation) nature is defined when D_{CT} falls below 1.6 Å.[29] On the other hand, Q_{CT} represents the charge transferred, which confirms to the combined change in ρ_+ or ρ_- over the volume on which electron densities expand. A value of Q_{CT} equal to 0 reflects a LE state, while 1 directs to a CT state. The final metric, $S_{\pm}$, accounts for the overlap between ρ_+ and ρ_-—an overlap of 1 suggests a LE state, while a value of 0 resembles a CT state. The density difference plots were generated using the VESTA software package.[67] The

https://doi.org/10.1021/acs.jpca.3c05056
J. Phys. Chem. A 2023, 127, 10393−10405

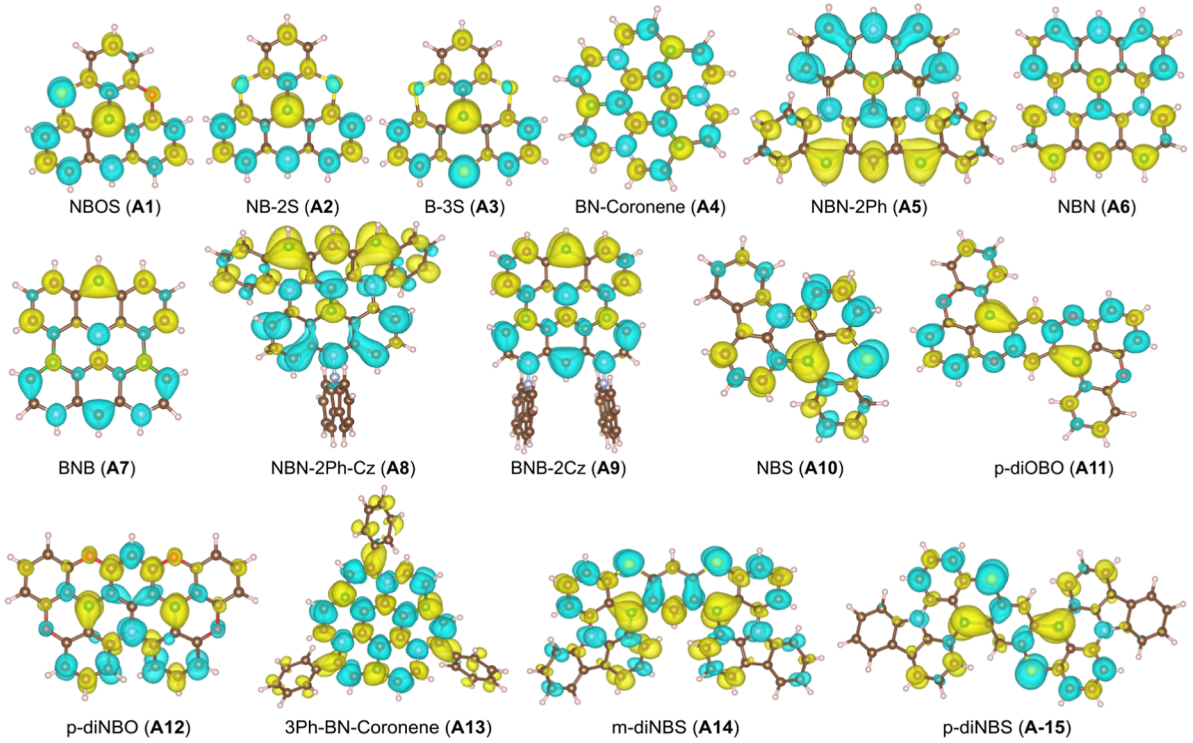

Figure 7. Difference density plots calculated for the designed emitter molecules for the first singlet-excited state (S_1), where blue and yellow lobes represent decreased and increased densities, respectively (isovalue = 0.001).

computed D_{CT}, Q_{CT}, and $S_{\pm}$ are summarized in Table S4 of the Supporting Information.

Figure 7 displays the computed difference density (Δ) plots for the investigated MR-TADF emitters. As can be seen from Figure 7, except for a few compounds, Δ is localized on neighboring atoms, confirming the short-range CT (SRCT) character of the excited states in the designed emitters. A closer inspection by comparing the corresponding D_{CT}, Q_{CT}, and $S_{\pm}$ values (see Table S4) guided us to distinguish the excited states' character in each emitter. For example, compounds A1, A2, and A3 are of similar type and are only different in terms of heteroatoms. As a result, the values of D_{CT}, Q_{CT}, and $S_{\pm}$ in these complexes differ marginally. A3 possesses the highest CT character percentage, as confirmed by the largest magnitudes of Q_{CT} and D_{CT}, and a lower overlap integral, $S_{\pm}$, than A1 and A2. Molecule A4 is symmetric; the density difference pattern is on the adjacent atoms, which implies a strong conjugation, and hence the overlap integral is almost closer to 1. Further, a lower value of D_{CT} and Q_{CT} ensures the SRCT character. An improved conjugation in the molecule also yielded the minimum ΔE_{ST} (0.063 eV) among the examined systems. On the other hand, complex A13 is the phenyl substitution of A4 to increase the conjugation further. The NICS(1) (1 Å above the ring center) results for the A4 and A13 complexes using their ground state and singlet and triplet geometries are summarized in Table S5 of Supporting Information. The calculated average NICS(1) value of the A13 complex (−20.523 ppm) is lower than that of the A4 complex (−14.545 ppm), suggesting its enhanced aromaticity and strong π-conjugation characteristics. Similar results have also been seen for the S_1 and T_1 geometries. However, it is apparent from Figure 7 that Δ is not distributed evenly on the phenyl rings, causing a reduction in the overlap integral to 0.94 from 0.99. Compounds A5, A6, and A7 differ from compound A4, as seen in their Δ plots. A5 exhibits a slightly separated distribution of Δ and not on the adjacent atoms—exhibiting a more CT-type character, which was further confirmed via its higher D_{CT} and Q_{CT} values compared to A6 and A7. A6 and A7 are different only in terms of B and N positions. Thus, there is little difference in their D_{CT} and Q_{CT}; however, both complexes lack adjacently located Δ, similar to A5. A8 and A9 are carbazole-substituted compounds A6 and A7, respectively. Both compounds show characteristics similar to those of their parent. As Figure 7 depicts, A10 exhibits SRCT nature. Compounds A11, A12, A14, and A15 are the fused type of structures. In almost all cases, the lobes are on the adjacent atoms; hence, all of these are of the SRCT type. The high value of overlap integral closer to 1 indicates the strong conjugation, and hence the exchange interactions become less, which causes ΔE_{ST} to be minimum.

Figure 8 displays an essential correlation between $S_{\pm}$ and D_{CT} of the S_1 states of the designed emitters where the color of each point represents the corresponding magnitude of ΔE_{ST}. As can be seen, there is an anticorrelation between D_{CT} and $S_{\pm}$, essentially yielding a negative correlation between the two metrics. The π-electron conjugation in the emitters is directly correlated to the overlap integral element. Hence, the strong π-conjugation of the emitters enhances the overlap integral and helps to reduce the magnitude of the exchange interaction (β). As shown in Figure 8, due to a lower magnitude of β, we observed a net reduction in the computed ΔE_{ST}. Thus, the present correlation provides a route to achieving a reduced ΔE_{ST} value in the MR-TADF complexes by enhancing the conjugation, which can be confirmed via the difference density analysis shown in Figure 7.

https://doi.org/10.1021/acs.jpca.3c05056
J. Phys. Chem. A 2023, 127, 10393−10405

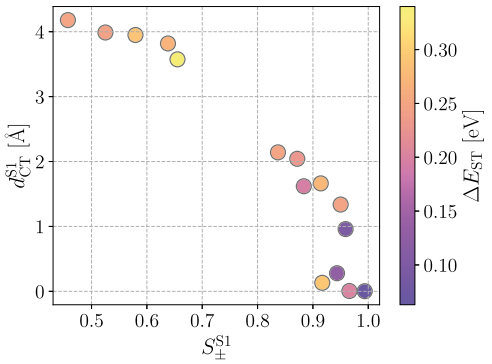

Figure 8. Correlation between the overlap $S_{\pm}^{S1}$ and D_{CT}^{S1} with the ΔE_{ST} values for the investigated MR-TADF systems. The color of each point defines the magnitude of ΔE_{ST}.

4. CONCLUSIONS

To summarize, we examined the electronic and photophysical properties of highly efficient MR-TADF-based emitters for future OLED applications employing an electronic structure framework. Our goal was to establish a computationally inexpensive route without compromising the accuracy for determining the singlet−triplet energy gap, ΔE_{ST}, which is one of the critical parameters governing the reverse intersystem crossing rates and, thus, the TADF efficiency. We computed ΔE_{ST} values from the difference between the vertical S_1-T_1 energy difference estimated employing the DLPNO-STEOM-CCSD method and the def2-SVP basis set. The DLPNO-STEOM-CCSD method accurately treats the excited-state characteristics by accounting for the higher-order excitations (singles and doubles).[40−45] Our results reveal that the predicted ΔE_{ST} value deviates only with a mean absolute deviation of 0.026 eV for the five experimentally investigated compounds, B1−B5 (see Figure 2).[14,15,18,28,46] Furthermore, the spin−orbit coupling between the S_1-T_1 transition and the associated reorganization energies was evaluated at the same level of theory. The rates of various photophysical events computed via eqs 1−5 further confirm the efficacy of our proposed computational approach and ensure its transferability to the study of future MR-TADF systems.

Later, we applied the abovementioned technique to examine ΔE_{ST}, rates of various photophysical events, and the TADF efficiencies of 15 newly designed MR-TADF emitters. Our design investigated the effects of N−B−N, O−B−O, and S−B−N functionalization on the core unit and side-chain functionalization. The designed set of molecules includes both monomeric (A1−A10) and fused (A11−A15) types of emitters (Figure 1). The results obtained via DLPNO-STEOM-CCSD calculations reveal that the designed systems possess a ΔE_{ST} value below 0.3 eV, except for one molecule with ΔE_{ST} of 0.34 eV. All devised complexes show excellent rates of prompt fluorescence (10^8 s^{-1}), reverse intersystem crossing (10^5 s^{-1} or higher), and delayed fluorescence (10^5 s^{-1} or higher). In addition, the predicted EQE and PLQY values yield values higher than 20 and 90%, respectively, in most compounds. A closer inspection further discloses the role of a balance between spin−orbit coupling ($H_{SO}^{S_1T_1}$) and ΔE_{ST} in achieving such high rates and, consequently, luminescent quantum efficiencies. Interestingly, the estimated emission wavelength confirmed that most conceived molecules emit in the blue region with an adequate to strong oscillator strength. Considering the lack of efficient blue emitters, these designed systems have significant relevance in practical applications in the OLED industry. Thus, the presented computational strategy opens an avenue to create and develop novel MR-TADF emitters for future applications.

■ ASSOCIATED CONTENT

Supporting Information

The Supporting Information is available free of charge at https://pubs.acs.org/doi/10.1021/acs.jpca.3c05056.

Description of details of computing quantum yields, data of photophysical parameters, and optimized geometries (PDF)

■ AUTHOR INFORMATION

Corresponding Author

Anirban Mondal − *Department of Chemistry, Indian Institute of Technology Gandhinagar, Gandhinagar, Gujarat 382355, India;* orcid.org/0000-0003-3029-8840; Email: amondal@iitgn.ac.in

Authors

Sanyam − *Department of Chemistry, Indian Institute of Technology Gandhinagar, Gandhinagar, Gujarat 382355, India;* orcid.org/0000-0001-7410-8207

Rudranarayan Khatua − *Department of Chemistry, Indian Institute of Technology Gandhinagar, Gandhinagar, Gujarat 382355, India*

Complete contact information is available at: https://pubs.acs.org/10.1021/acs.jpca.3c05056

Author Contributions

†Sanyam and R.K. contributed equally to this work.

Notes

The authors declare no competing financial interest.

■ ACKNOWLEDGMENTS

The authors gratefully acknowledge the Indian Institute of Technology Gandhinagar, India, for providing research facilities and support. A.M. acknowledges the SERB (SRG/2022/001532) project for funding. Sanyam thanks the Council of Scientific and Industrial Research (CSIR), India, for a fellowship. The authors thank PARAM Ananta for computational resources.

■ REFERENCES

(1) Baldo, M. A.; O'Brien, D. F.; You, Y.; Shoustikov, A.; Sibley, S.; Thompson, M. E.; Forrest, S. R. Highly efficient phosphorescent emission from organic electroluminescent devices. *Nature* **1998**, *395*, 151−154.

(2) Baldo, M. A.; Lamansky, S.; Burrows, P. E.; Thompson, M. E.; Forrest, S. R. Very high-efficiency green organic light-emitting devices based on electrophosphorescence. *Appl. Phys. Lett.* **1999**, *75*, 4−6.

(3) Reineke, S.; Lindner, F.; Schwartz, G.; Seidler, N.; Walzer, K.; Lüssem, B.; Leo, K. White organic light-emitting diodes with fluorescent tube efficiency. *Nature* **2009**, *459*, 234−238.

(4) Endo, A.; Sato, K.; Yoshimura, K.; Kai, T.; Kawada, A.; Miyazaki, H.; Adachi, C. Efficient up-conversion of triplet excitons into a singlet state and its application for organic light emitting diodes. *Appl. Phys. Lett.* **2011**, *98*, 083302.

(5) Uoyama, H.; Goushi, K.; Shizu, K.; Nomura, H.; Adachi, C. Highly efficient organic light-emitting diodes from delayed fluorescence. *Nature* **2012**, *492*, 234−238.

(6) Liu, Y.; Li, C.; Ren, Z.; Yan, S.; Bryce, M. R. All-organic thermally activated delayed fluorescence materials for organic light-emitting diodes. *Nat. Rev. Mater.* **2018**, *3*, 18020.
(7) Xu, Y.; Cheng, Z.; Li, Z.; Liang, B.; Wang, J.; Wei, J.; Zhang, Z.; Wang, Y. Molecular-structure and device-configuration optimizations toward highly efficient green electroluminescence with narrowband emission and high color purity. *Adv. Opt. Mater.* **2020**, *8*, 1902142.
(8) Xu, Y.; Li, C.; Li, Z.; Wang, Q.; Cai, X.; Wei, J.; Wang, Y. Constructing Charge-Transfer Excited States Based on Frontier Molecular Orbital Engineering: Narrowband Green Electroluminescence with High Color Purity and Efficiency. *Angew. Chem., Int. Ed.* **2020**, *59*, 17442−17446.
(9) Izumi, S.; Higginbotham, H. F.; Nyga, A.; Stachelek, P.; Tohnai, N.; Silva, P. d.; Data, P.; Takeda, Y.; Minakata, S. Thermally activated delayed fluorescent donor−acceptor−donor−acceptor π-conjugated macrocycle for organic light-emitting diodes. *J. Am. Chem. Soc.* **2020**, *142*, 1482−1491.
(10) Goushi, K.; Yoshida, K.; Sato, K.; Adachi, C. Organic light-emitting diodes employing efficient reverse intersystem crossing for triplet-to-singlet state conversion. *Nat. Photonics* **2012**, *6*, 253−258.
(11) Stachelek, P.; Ward, J. S.; dos Santos, P. L.; Danos, A.; Colella, M.; Haase, N.; Raynes, S. J.; Batsanov, A. S.; Bryce, M. R.; Monkman, A. P. Molecular Design Strategies for Color Tuning of Blue TADF Emitters. *ACS Appl. Mater. Interfaces* **2019**, *11*, 27125−27133.
(12) Im, Y.; Kim, M.; Cho, Y. J.; Seo, J.-A.; Yook, K. S.; Lee, J. Y. Molecular Design Strategy of Organic Thermally Activated Delayed Fluorescence Emitters. *Chem. Mater.* **2017**, *29*, 1946−1963.
(13) Wong, M. Y.; Zysman-Colman, E. Purely Organic Thermally Activated Delayed Fluorescence Materials for Organic Light-Emitting Diodes. *Adv. Mater.* **2017**, *29*, 1605444.
(14) Hatakeyama, T.; Shiren, K.; Nakajima, K.; Nomura, S.; Nakatsuka, S.; Kinoshita, K.; Ni, J.; Ono, Y.; Ikuta, T. Ultrapure blue thermally activated delayed fluorescence molecules: efficient HOMO−LUMO separation by the multiple resonance effect. *Adv. Mater.* **2016**, *28*, 2777−2781.
(15) Oda, S.; Kawakami, B.; Kawasumi, R.; Okita, R.; Hatakeyama, T. Multiple resonance effect-induced sky-blue thermally activated delayed fluorescence with a narrow emission band. *Org. Lett.* **2019**, *21*, 9311−9314.
(16) Northey, T.; Penfold, T. The intersystem crossing mechanism of an ultrapure blue organoboron emitter. *Org. Electron.* **2018**, *59*, 45−48.
(17) Pershin, A.; Hall, D.; Lemaur, V.; Sancho-Garcia, J.-C.; Muccioli, L.; Zysman-Colman, E.; Beljonne, D.; Olivier, Y. Highly emissive excitons with reduced exchange energy in thermally activated delayed fluorescent molecules. *Nat. Commun.* **2019**, *10*, 597.
(18) Zhang, Y.; Zhang, D.; Wei, J.; Liu, Z.; Lu, Y.; Duan, L. Multi-resonance induced thermally activated delayed fluorophores for narrowband green OLEDs. *Angew. Chem., Int. Ed.* **2019**, *58*, 16912−16917.
(19) Zhang, Y.; Zhang, D.; Wei, J.; Hong, X.; Lu, Y.; Hu, D.; Li, G.; Liu, Z.; Chen, Y.; Duan, L. Achieving pure green electroluminescence with CIEy of 0.69 and EQE of 28.2% from an aza-fused multi-resonance emitter. *Angew. Chem.* **2020**, *132*, 17652−17656.
(20) Han, S. H.; Jeong, J. H.; Yoo, J. W.; Lee, J. Y. Ideal blue thermally activated delayed fluorescence emission assisted by a thermally activated delayed fluorescence assistant dopant through a fast reverse intersystem crossing mediated cascade energy transfer process. *J. Mater. Chem. C* **2019**, *7*, 3082−3089.
(21) Matsui, K.; Oda, S.; Yoshiura, K.; Nakajima, K.; Yasuda, N.; Hatakeyama, T. One-Shot Multiple Borylation toward BN-Doped Nanographenes. *J. Am. Chem. Soc.* **2018**, *140*, 1195−1198.
(22) Yang, M.; Park, I. S.; Yasuda, T. Full-Color, Narrowband, and High-Efficiency Electroluminescence from Boron and Carbazole Embedded Polycyclic Heteroaromatics. *J. Am. Chem. Soc.* **2020**, *142*, 19468−19472.
(23) Hall, D.; Suresh, S. M.; dos Santos, P. L.; Duda, E.; Bagnich, S.; Pershin, A.; Rajamalli, P.; Cordes, D. B.; Slawin, A. M. Z.; Beljonne, D.; Köhler, A.; Samuel, I. D. W.; Olivier, Y.; Zysman-Colman, E. Improving Processability and Efficiency of Resonant TADF Emitters: A Design Strategy. *Adv. Opt. Mater.* **2020**, *8*, 1901627.
(24) Qiu, X.; Tian, G.; Lin, C.; Pan, Y.; Ye, X.; Wang, B.; Ma, D.; Hu, D.; Luo, Y.; Ma, Y. Narrowband Emission from Organic Fluorescent Emitters with Dominant Low-Frequency Vibronic Coupling. *Adv. Opt. Mater.* **2021**, *9*, 2001845.
(25) Lee, Y.-T.; Chan, C.-Y.; Tanaka, M.; Mamada, M.; Balijapalli, U.; Tsuchiya, Y.; Nakanotani, H.; Hatakeyama, T.; Adachi, C. Investigating HOMO Energy Levels of Terminal Emitters for Realizing High-Brightness and Stable TADF-Assisted Fluorescence Organic Light-Emitting Diodes. *Adv. Electron. Mater.* **2021**, *7*, 2001090.
(26) Huang, F.; Wang, K.; Shi, Y.-Z.; Fan, X.-C.; Zhang, X.; Yu, J.; Lee, C.-S.; Zhang, X.-H. Approaching Efficient and Narrow RGB Electroluminescence from D−A-Type TADF Emitters Containing an Identical Multiple Resonance Backbone as the Acceptor. *ACS Appl. Mater. Interfaces* **2021**, *13*, 36089−36097.
(27) Oda, S.; Sugitani, T.; Tanaka, H.; Tabata, K.; Kawasumi, R.; Hatakeyama, T. Development of Pure Green Thermally Activated Delayed Fluorescence Material by Cyano Substitution. *Adv. Mater.* **2022**, *34*, 2201778.
(28) Park, J.; Lim, J.; Lee, J. H.; Jang, B.; Han, J. H.; Yoon, S. S.; Lee, J. Y. Asymmetric Blue Multiresonance TADF Emitters with a Narrow Emission Band. *ACS Appl. Mater. Interfaces* **2021**, *13*, 45798−45805.
(29) Hall, D.; Stavrou, K.; Duda, E.; Danos, A.; Bagnich, S.; Warriner, S.; Slawin, A. M. Z.; Beljonne, D.; Köhler, A.; Monkman, A.; Olivier, Y.; Zysman-Colman, E. Diindolocarbazole − achieving multiresonant thermally activated delayed fluorescence without the need for acceptor units. *Mater. Horiz.* **2022**, *9*, 1068−1080.
(30) Gao, Y.; Pan, Q.-Q.; Zhao, L.; Geng, Y.; Su, T.; Gao, T.; Su, Z.-M. Realizing performance improvement of blue thermally activated delayed fluorescence molecule DABNA by introducing substituents on the para-position of boron atom. *Chem. Phys. Lett.* **2018**, *701*, 98−102.
(31) Lin, L.; Fan, J.; Cai, L.; Wang, C.-K. Excited state dynamics of new-type thermally activated delayed fluorescence emitters: theoretical view of light-emitting mechanism. *Mol. Phys.* **2018**, *116*, 19−28.
(32) Samanta, P. K.; Kim, D.; Coropceanu, V.; Brédas, J. L. Up-Conversion Intersystem Crossing Rates in Organic Emitters for Thermally Activated Delayed Fluorescence: Impact of the Nature of Singlet vs Triplet Excited States. *J. Am. Chem. Soc.* **2017**, *139*, 4042−4051.
(33) Suresh, S. M.; Duda, E.; Hall, D.; Yao, Z.; Bagnich, S.; Slawin, A. M. Z.; Bässler, H.; Beljonne, D.; Buck, M.; Olivier, Y.; Köhler, A.; Zysman-Colman, E. A Deep Blue B,N-Doped Heptacene Emitter That Shows Both Thermally Activated Delayed Fluorescence and Delayed Fluorescence by Triplet−Triplet Annihilation. *J. Am. Chem. Soc.* **2020**, *142*, 6588−6599.
(34) Nooijen, M.; Bartlett, R. J. Similarity transformed equation-of-motion coupled-cluster theory: Details, examples, and comparisons. *J. Chem. Phys.* **1997**, *107*, 6812−6830.
(35) Nooijen, M.; Bartlett, R. J. A new method for excited states: Similarity transformed equation-of-motion coupled-cluster theory. *J. Chem. Phys.* **1997**, *106*, 6441−6448.
(36) Riplinger, C.; Neese, F. An efficient and near linear scaling pair natural orbital based local coupled cluster method. *J. Chem. Phys.* **2013**, *138*, 034106.
(37) Riplinger, C.; Sandhoefer, B.; Hansen, A.; Neese, F. Natural triple excitations in local coupled cluster calculations with pair natural orbitals. *J. Chem. Phys.* **2013**, *139*, 134101.
(38) Dutta, A. K.; Nooijen, M.; Neese, F.; Izsák, R. Automatic active space selection for the similarity transformed equations of motion coupled cluster method. *J. Chem. Phys.* **2017**, *146*, 074103.
(39) Dutta, A. K.; Nooijen, M.; Neese, F.; Izsák, R. Exploring the accuracy of a low scaling similarity transformed equation of motion method for vertical excitation energies. *J. Chem. Theory Comput.* **2018**, *14*, 72−91.
(40) Berraud-Pache, R.; Neese, F.; Bistoni, G.; Izsák, R. Unveiling the photophysical properties of boron-dipyrromethene dyes using a

https://doi.org/10.1021/acs.jpca.3c05056
J. Phys. Chem. A 2023, 127, 10393−10405

new accurate excited state coupled cluster method. *J. Chem. Theory Comput.* **2020**, *16*, 564−575.
(41) Berraud-Pache, R.; Neese, F.; Bistoni, G.; Izsak, R. Computational design of near-infrared fluorescent organic dyes using an accurate new wave function approach. *J. Phys. Chem. Lett.* **2019**, *10*, 4822−4828.
(42) Kozma, B.; Tajti, A.; Demoulin, B.; Izsák, R.; Nooijen, M.; Szalay, P. G. A new benchmark set for excitation energy of charge transfer states: systematic investigation of coupled cluster type methods. *J. Chem. Theory Comput.* **2020**, *16*, 4213−4225.
(43) Bhattacharyya, K. Can TDDFT render the electronic excited states ordering of Azine derivative? A closer investigation with DLPNO-STEOM-CCSD. *Chem. Phys. Lett.* **2021**, *779*, 138827.
(44) Pratik, S. M.; Coropceanu, V.; Bredas, J.-L. Enhancement of thermally activated delayed fluorescence (TADF) in multi-resonant emitters via control of chalcogen atom embedding. *Chem. Mater.* **2022**, *34*, 8022−8030.
(45) Pratik, S. M.; Coropceanu, V.; Bredas, J.-L. Purely organic emitters for multiresonant thermally activated delay fluorescence: design of highly efficient sulfur and selenium derivatives. *ACS Mater. Lett.* **2022**, *4*, 440−447.
(46) Xiong, X.; Cheng, Y.-C.; Wang, K.; Yu, J.; Zhang, X.-H. A comparative study of two multi-resonance TADF analogous materials integrating chalcogen atoms of different periods. *Mater. Chem. Front.* **2023**, *7*, 929−936.
(47) Kerru, N.; Gummidi, L.; Bhaskaruni, S. V.; Maddila, S. N.; Singh, P.; Jonnalagadda, S. B. A comparison between observed and DFT calculations on structure of 5-(4-chlorophenyl)-2-amino-1, 3, 4-thiadiazole. *Sci. Rep.* **2019**, *9*, 19280.
(48) Halsey-Moore, C.; Jena, P.; McLeskey, J. T. Tuning range-separated DFT functionals for modeling the peak absorption of MEH-PPV polymer in various solvents. *Comput. Theor. Chem.* **2019**, *1162*, 112506.
(49) Barone, V.; Cossi, M. Quantum calculation of molecular energies and energy gradients in solution by a conductor solvent model. *J. Phys. Chem. A* **1998**, *102*, 1995−2001.
(50) Frisch, M. J.; et al. *Gaussian 09*; Gaussian, Inc.: Wallingford, CT, 2009.
(51) Neese, F. The ORCA program system. *Wiley Interdiscip. Rev.: Comput. Mol. Sci.* **2012**, *2*, 73−78.
(52) Chen, F.; Zhao, L.; Wang, X.; Yang, Q.; Li, W.; Tian, H.; Shao, S.; Wang, L.; Jing, X.; Wang, F. Novel boron-and sulfur-doped polycyclic aromatic hydrocarbon as multiple resonance emitter for ultrapure blue thermally activated delayed fluorescence polymers. *Sci. China Chem.* **2021**, *64*, 547−551.
(53) Kitamoto, Y.; Suzuki, T.; Miyata, Y.; Kita, H.; Funaki, K.; Oi, S. The first synthesis and X-ray crystallographic analysis of an oxygen-bridged planarized triphenylborane. *Chem. Commun.* **2016**, *52*, 7098−7101.
(54) Hirai, H.; Nakajima, K.; Nakatsuka, S.; Shiren, K.; Ni, J.; Nomura, S.; Ikuta, T.; Hatakeyama, T. One-Step Borylation of 1, 3-Diaryloxybenzenes Towards Efficient Materials for Organic Light-Emitting Diodes. *Angew. Chem., Int. Ed.* **2015**, *54*, 13581−13585.
(55) Zhang, K.; Liu, J.; Zhang, Y.; Fan, J.; Wang, C.-K.; Lin, L. Theoretical Study of the Mechanism of Aggregation-Caused Quenching in Near-Infrared Thermally Activated Delayed Fluorescence Molecules: Hydrogen-Bond Effect. *J. Phys. Chem. C* **2019**, *123*, 24705−24713.
(56) Xu, S.; Yang, Q.; Wan, Y.; Chen, R.; Wang, S.; Si, Y.; Yang, B.; Liu, D.; Zheng, C.; Huang, W. Predicting intersystem crossing efficiencies of organic molecules for efficient thermally activated delayed fluorescence. *J. Mater. Chem. C* **2019**, *7*, 9523−9530.
(57) Viani, L.; Olivier, Y.; Athanasopoulos, S.; da Silva Filho, D. A.; Hulliger, J.; Brédas, J.; Gierschner, J.; Cornil, J. Theoretical Characterization of Charge Transport in One-Dimensional Collinear Arrays of Organic Conjugated Molecules. *ChemPhysChem* **2010**, *11*, 1062−1068.
(58) Shakeel, U.; Singh, J. Study of processes of reverse intersystem crossing (RISC) and thermally activated delayed fluorescence (TADF) in organic light emitting diodes (OLEDs). *Org. Electron.* **2018**, *59*, 121−124.
(59) Hall, D.; Sancho-García, J. C.; Pershin, A.; Ricci, G.; Beljonne, D.; Zysman-Colman, E.; Olivier, Y. Modeling of Multiresonant Thermally Activated Delayed Fluorescence Emitters-Properly Accounting for Electron Correlation Is Key. *J. Chem. Theory Comput.* **2022**, *18*, 4903−4918.
(60) Shizu, K.; Kaji, H. Comprehensive understanding of multiple resonance thermally activated delayed fluorescence through quantum chemistry calculations. *Commun. Chem.* **2022**, *5*, 53.
(61) Shi, B.; Nachtigallová, D.; Aquino, A. J.; Machado, F. B.; Lischka, H. High-level theoretical benchmark investigations of the UV-vis absorption spectra of paradigmatic polycyclic aromatic hydrocarbons as models for graphene quantum dots. *J. Chem. Phys.* **2019**, *150*, 124302.
(62) Itoh, T. Fluorescence and phosphorescence from higher excited states of organic molecules. *Chem. Rev.* **2012**, *112*, 4541−4568.
(63) O'boyle, N. M.; Tenderholt, A. L.; Langner, K. M. Cclib: a library for package-independent computational chemistry algorithms. *J. Comput. Chem.* **2008**, *29*, 839−845.
(64) Hilgevoord, J. The uncertainty principle for energy and time. *Am. J. Phys.* **1996**, *64*, 1451−1456.
(65) Naveen, K. R.; Yang, H. I.; Kwon, J. H. Double boron-embedded multiresonant thermally activated delayed fluorescent materials for organic light-emitting diodes. *Commun. Chem.* **2022**, *5*, 149.
(66) Lu, T.; Chen, F. Multiwfn: A multifunctional wavefunction analyzer. *J. Comput. Chem.* **2012**, *33*, 580−592.
(67) Momma, K.; Izumi, F. VESTA3 for three-dimensional visualization of crystal, volumetric and morphology data. *J. Appl. Crystallogr.* **2011**, *44*, 1272−1276.

https://doi.org/10.1021/acs.jpca.3c05056
J. Phys. Chem. A 2023, 127, 10393−10405